On the intensity ratio variation of the Si IV 1394/1403 Å lines during solar flares

Resonance scattering and opacity effects

Hao-Cheng Yu[1,2], J. Hong[1,2], and M. D. Ding[1,2]

[1] School of Astronomy and Space Science, Nanjing University, 163 Xianlin Road, Nanjing 210023, PR China
e-mail: `jiehong@nju.edu.cn`
[2] Key Laboratory for Modern Astronomy and Astrophysics (Nanjing University), Ministry of Education, Nanjing 210023, 163 Xianlin Road, PR China

ABSTRACT

Context. The Si IV lines at 1394 Å and 1403 Å form in the solar atmosphere at a temperature of $\sim 10^{4.8}$ K. They are usually considered optically thin, but their opacity can be enhanced during solar flares. Traditionally, the intensity ratio of these lines are used as an indicator of the optical thickness. However, observations have shown a wavelength-dependent intensity ratio profile $r(\Delta\lambda)$ of the the 1394 Å to 1403 Å lines.

Aims. We aim to study the variation of the intensity ratio profile in solar flares and the physical reasons behind it.

Methods. The Si IV lines and their intensity ratio profiles are calculated from the one-dimensional radiative hydrodynamics flare model with non-thermal electron heating.

Results. During flares, $r(\Delta\lambda)$ is smaller than 2 at the line core but larger than 2 at the line wings. We attribute the deviation of the ratio from 2 to two effects: the resonance scattering effect and the opacity effect. Resonance scattering increases the population ratio of the upper levels of the two lines, and as a result, increases $r(\Delta\lambda)$, in all wavelengths. The opacity effect decreases $r(\Delta\lambda)$, especially at the line core where the opacity is larger. These two effects compete with each other and cause the U-shape of $r(\Delta\lambda)$.

Key words. sun: chromosphere – line: profiles – radiative transfer – opacity

1. Introduction

The transition region (TR) is a thin layer between the chromosphere and the corona, where the physical quantities change dramatically in the Sun. The temperature could change by several orders of magnitude, and a number of emission lines form in the TR, such as the Si IV, C IV, O IV, and Ne VII lines, which could reveal the dynamic properties of local plasma. The Si IV resonance lines at 1394 Å and 1403 Å are two typical TR lines with a formation temperature of $\sim 10^{4.8}$ K. It is generally accepted that photons generated in the TR are able to escape from the solar surface without absorption or scattering; that is, these lines are usually considered optically thin. Under the optically thin assumption, Mathioudakis et al. (1999) indicated that, for pairs of resonance lines such as Si IV 1394/1403 Å and C IV 1548/1551 Å which share the same lower level but different upper levels, the ratio of the line intensities is exactly the ratio of the oscillator strengths of the two lines. This ratio is 0.52:0.26=2:1 for the Si IV 1394/1403 Å lines (Maniak et al. 1993). Usually, a decrease from 2 implies that there is an opacity effect along the line of sight.

During heating events like transient brightenings in the transition region or solar flares, the atmosphere is heated to a high temperature where the Si IV lines could be significantly enhanced. Recent works suggested that the optically thin assumption of the Si IV lines does not hold in some cases. Yan et al. (2015) found the self-absorption effect on both Si IV lines for the first time. They found that the intensity ratio is reduced to

1.7∼2. The same effect has also been reported in Nelson et al. (2017). Tripathi et al. (2020) studied the distribution of intensity ratios in active regions. They concluded that there are a considerable number of pixels where the intensity ratio deviates from 2, especially in the early phases of flares and in parts of flare ribbons. Recent radiative hydrodynamic simulations indicated that the two Si IV lines might not be optically thin in flare conditions (Kerr et al. 2019), where the intensity ratio varies from 1.8 to 2.3.

It should be pointed out that the intensity ratio could also be larger than 2 in many observations (Tripathi et al. 2020; Zhou et al. 2022), where the opacity effect fails to explain. Previous studies attributed this to the result of resonance scattering, which implies that a stronger resonance scattering yields a larger intensity ratio (Gontikakis & Vial 2018; Gontikakis et al. 2013).

The above mentioned intensity ratio usually refers to the ratio of wavelength-integrated intensity $R = \int I_{1394\text{Å}}(\lambda)\mathrm{d}\lambda / \int I_{1403\text{Å}}(\lambda)\mathrm{d}\lambda$ as adopted in previous studies. However, considering that the opacity at the line core is much larger than that at the line wings, the intensity ratio may also vary from the line core to the line wings. Zhou et al. (2022) focused on the wavelength-dependent intensity ratio profile $r(\Delta\lambda) = I_{1394\text{Å}}(\Delta\lambda)/I_{1403\text{Å}}(\Delta\lambda)$. They found that at the flare ribbons, $r(\Delta\lambda)$ is less than 2 at the line core and larger than 2 at the line wings, while the ratio of the integrated intensity is still close to 2. It is suggested that the intensity ratio profile $r(\Delta\lambda)$ serves as a better proxy of the line opacity. Thus, the variation of $r(\Delta\lambda)$ along wavelength deserves further investigation.

In this paper, we study the intensity ratio profile $r(\Delta\lambda)$ of the Si IV resonance lines in one-dimensional radiative hydrodynamic flare models. We examine the variation of the intensity ratio along wavelength and explore possible physical mechanisms. The flare models and calculation of the Si IV lines are briefly described in Section 2. The spectral line profiles and intensity ratio profiles $r(\Delta\lambda)$ are shown in Section 3. Reasons for the variation of $r(\Delta\lambda)$ are discussed in Section 4. Finally we make conclusions in Section 5.

2. Method

The one-dimensional radiative hydrodynamics code RADYN was first used to study shocks in the chromosphere (Carlsson & Stein 1992, 1997, 1995), but now it is more often employed for the response of the solar atmosphere during flares (Allred et al. 2015). The conservation equations of mass, momentum, energy and charge coupled with atom level population equations and radiative transfer equations are solved in a 1D plane-parallel atmosphere, on an adaptive grid (Dorfi & Drury 1987). The initial atmosphere is based on the VAL3C model, with a 10 Mm semicircular flare loop. The loop-top temperature is 10 MK. To simulate the heating by flares, a high energy non-thermal electron beam is injected from the loop top, and then moves downward along the flare loop. A set of three parameters describes the power-law energy distribution of non-thermal electrons: the cut-off energy E_c, the spectral index δ, and the energy flux F. The former two parameters are fixed in each simulation run, while the energy flux rises with time linearly to a peak F_{peak} at 10 s, and then falls linearly to zero at 20 s. We have made a grid of 25 simulations by varying E_c from 5 to 25 keV and varying δ from 3 to 7, where F_{peak} is fixed at 10^{10} erg s^{-1} cm^{-2}. We find that a large value of E_c causes stronger heating at large column depth and a small value of δ makes the heating more concentrated. The variation of E_c and δ causes different heating rates with height and different intensities of profiles, while the distribution of line ratios and population ratios do not change qualitatively. Thus, we only show three typical cases here. Besides, we also show another simulation with a larger F_{peak} (10^{11} erg s^{-1} cm^{-2}) where the line profiles show central reversals. These four cases are described in Table 1, where the notations are the same as that in Hong et al. (2022), and the other 22 cases are listed in Appendix A. The heating rate of the flaring atmosphere is calculated with the Fokker-Plank approach. We run each simulation for 20 s.

Table 1. Parameters of flare models*

Case	F_{peak}/[erg s^{-1} cm^{-2}]	E_c/[keV]	δ
f10E15d3	10^{10}	15	3
f10E25d3	10^{10}	25	3
f10E25d7	10^{10}	25	7
f11E25d3	10^{11}	25	3

* Details for other simulation runs are included in Appendix A.

The minority species version of the code (MS_RADYN) is employed to calculate the Si IV lines which do not contribute significantly to the atmosphere. We follow the atmosphere of the main run, and solve the level populations and radiative transfer equations for the silicon atom only (Kerr et al. 2019). The Si model atom is the same as in Kerr et al. (2019). The snapshot of the simulations are saved every 0.1 s.

3. Result

3.1. The intensity ratio profile $r(\Delta\lambda)$

The time evolution of the Si IV intensity profiles and the intensity ratio profile $r(\Delta\lambda)$ for the four simulation cases are shown in Figure 1. At each wavelength, we have subtracted the averaged intensity value at far wings (± 1 Å) from the profile to eliminate the influence of the continuum. Such a subtraction is done for every timestep. From the intensity profiles one can see clearly that the Si IV intensity is enhanced after a certain time of heating, when sufficient energy is deposited in the upper chromosphere ($1.4 - 1.8$ Mm) and the number of Si IV atoms is increased. For the first three cases, the line profiles show a single peak that is gradually blueshifted, indicating the upflow of chromospheric evaporation (Li et al. 2019; Kerr et al. 2019). Comparing the first three panels, we can find some differences in the profiles when changing the spectral index δ and the cut-off energy E_c. A larger value of δ and a smaller value of E_c mean that the electrons are mostly distributed in the lower-energy part, which cause faster and stronger heating at a low column depth, corresponding to the earlier enhancement and greater intensity, respectively. We note that for Case f10E25d7, the top part of the chromosphere is undisturbed and becomes trapped between the heated chromosphere and the transition region, forming a "chromospheric bubble" (Reid et al. 2020). For Case f11E25d3 (Figure 2), the line profiles show multi-peaks from $t = 5$ s and last for the whole flare. The central reversal caused by absorption in the line core suggests a large opacity at -0.5 Å, and an additional red component at around 0.8 Å serves as a result of condensation downflows (Tian et al. 2022).

The intensity ratio profile keeps close to 2 before the obvious enhancement of the Si IV line profiles. A variation of the ratio at different wavelengths is clearly shown, where the ratio at the line wings is generally larger than 2, while the ratio at the line core is generally smaller than 2. For each intensity ratio profile, we choose three specific wavelength positions to represent the line core ($\Delta\lambda_c$), the blue wing ($\Delta\lambda_b$), and the red wing ($\Delta\lambda_r$), respectively, which are overplotted in Figure 1. The centroid of the Si IV 1403 Å intensity profile is chosen as $\Delta\lambda_c$. The values of $\Delta\lambda_b$ and $\Delta\lambda_r$ are specifically chosen so that $\int_{\Delta\lambda_{\mathrm{min}}}^{\Delta\lambda_b} I_{1403\text{Å}}\mathrm{d}\lambda = \int_{\Delta\lambda_r}^{\Delta\lambda_{\mathrm{max}}} I_{1403\text{Å}}\mathrm{d}\lambda = 0.01 \int_{\Delta\lambda_{\mathrm{min}}}^{\Delta\lambda_{\mathrm{max}}} I_{1403\text{Å}}\mathrm{d}\lambda$, where the integration range $[\Delta\lambda_{\mathrm{min}}, \Delta\lambda_{\mathrm{max}}]$ is [-0.5 Å, 0.5 Å]. In Figure 3 we show the ratio of wavelength-integrated intensity R and the wavelength-dependent ratio $r(\Delta\lambda)$ at these wavelength positions. It is obvious that after a certain time of heating, $r(\Delta\lambda_b)$ and $r(\Delta\lambda_r)$ are generally larger than R, and $r(\Delta\lambda_c)$ tends to be smaller than R. The value of $r(\Delta\lambda)$ can reach as high as 3.5 at the line wings and as low as 1.5 at the line center, while the value of R is still close to 2 owing to an integration effect. The variation behavior of $r(\Delta\lambda)$ and the quantity of R are quite similar to observations at flare ribbons (Zhou et al. 2022).

3.2. The optical thickness

Previous studies suggested that the opacity cannot be neglected when we calculate the Si IV resonance lines during strong flares (Kerr et al. 2019). To understand the opacity effect in line formation, calculation of the contribution function is a useful way (Caccin et al. 1977; Magain 1986). The analytic solution of the radiative transfer equation is

$$I_{\lambda,\mu} = \int \frac{1}{\mu} S_\lambda(\tau_\lambda) e^{-\tau_\lambda/\mu} \mathrm{d}\tau_\lambda, \tag{1}$$
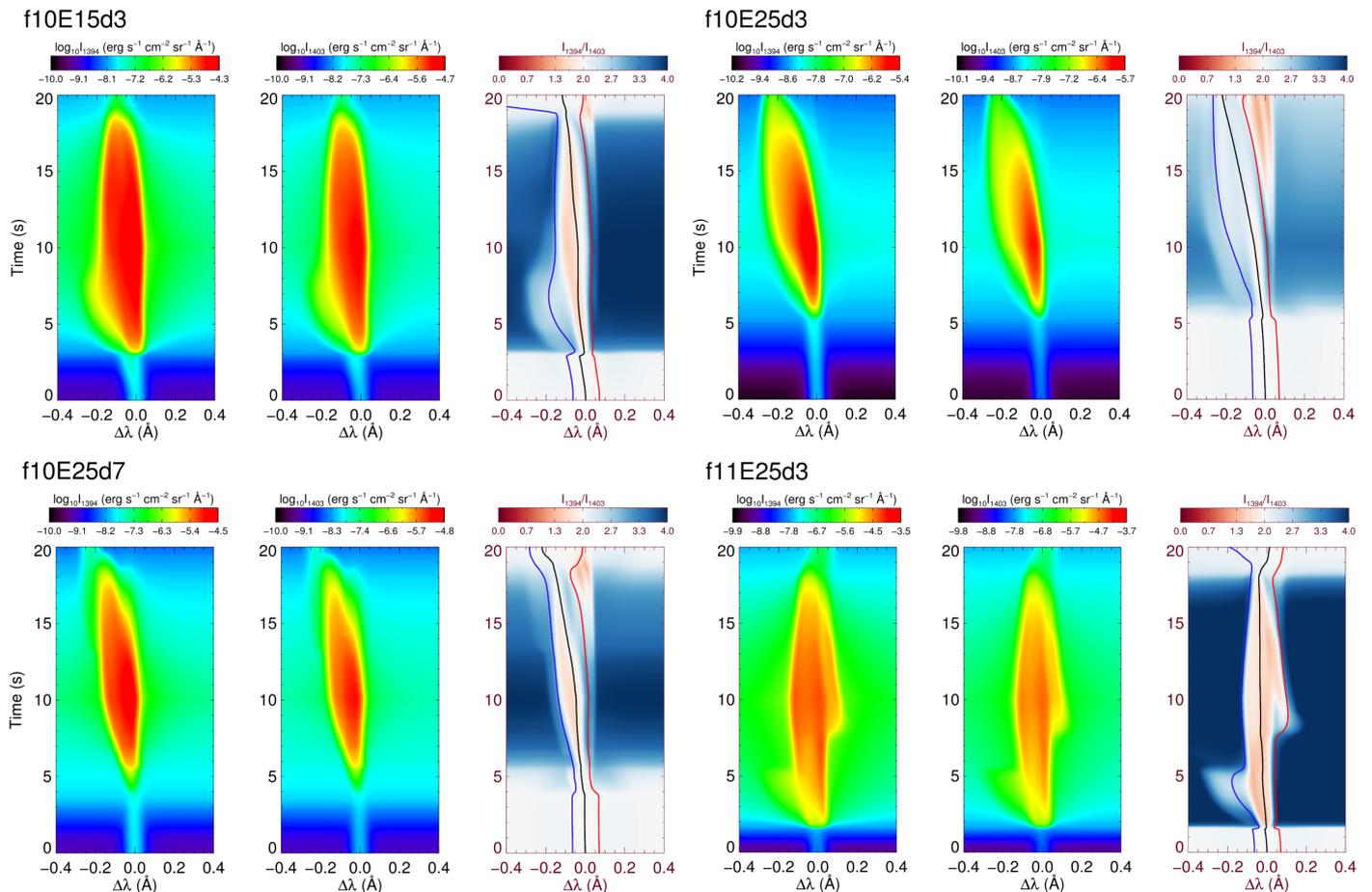
Fig. 1. Time evolution of the Si IV line profiles (1394 Å on the left) and the intensity ratio profiles $r(\Delta\lambda)$ in all four flare models. Black, red and blue lines show wavelength positions that are specifically chosen to represent the line core ($\Delta\lambda_c$), the red wing ($\Delta\lambda_r$) and the blue wing ($\Delta\lambda_b$) at each time, respectively, which are defined in Section 3.1.
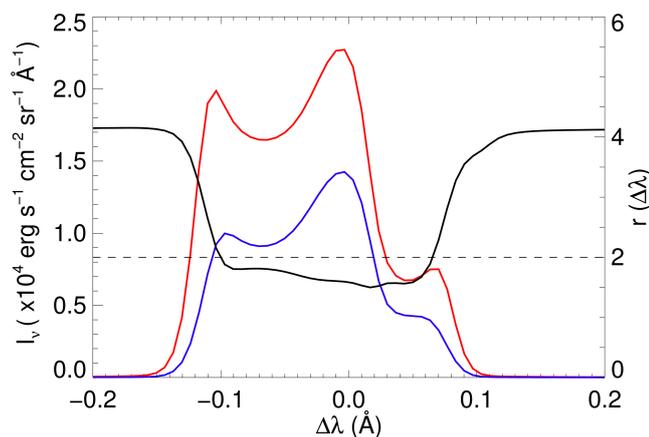
Fig. 2. Line profiles of Si IV 1394 Å (red line), Si IV 1403 Å (blue line) and the intensity ratio profile $r(\Delta\lambda)$ (black line) at $t = 10$ s for Case f11E25d3.

where $\mu = \cos\theta$ and θ is the angle between the observer and the vertical direction. We use $\mu \approx 1$ in this work. $S_\lambda(\tau_\lambda)$ and τ_λ are the source function and the optical depth, respectively. We use the variable dz (geometrical depth) instead of dτ_λ to get another form:

$$I_\lambda = \int C_\lambda \mathrm{d}z = \int j_\lambda(z)\mathrm{e}^{-\tau_\lambda(z)}\mathrm{d}z, \qquad (2)$$

where $j_\lambda(z)$ is the emissivity, and C_λ is the contribution function with respect to wavelength per height. We can get the emergent intensity by integrating the contribution function along the light path.

Hereby we take Case f10E25d3 as an example. The results from other three cases do not show qualitative differences, and are together shown in Appendix B. Figure 4 shows the contribution function of the Si IV 1403 Å line. At each wavelength, the contribution function mainly peaks at two heights, contributed by continuum emission from the temperature minimum region and line emission in the upper chromosphere and the transition region, respectively. At $t = 0$ s, the contribution function at the Si IV 1403 Å line center gathers at $z \approx 1.8$ Mm, indicating that the line is mainly formed in the transition region.

The height where $\tau_\lambda = 1$ is at around 0.5 Mm at this moment, where the continuum is formed, far lower than the transition region. The opacity at the line formation region is quite small where the absorption can be neglected safely, and thus the line can be regarded as optically thin. At $t = 10$ s, the region between 1.5 Mm and 2 Mm that is heated intensively now contributes mostly to the line emission. Meanwhile, the $\tau_\lambda = 1$ curve also rises to $z \approx 1.6$ Mm around the line core, which implies that
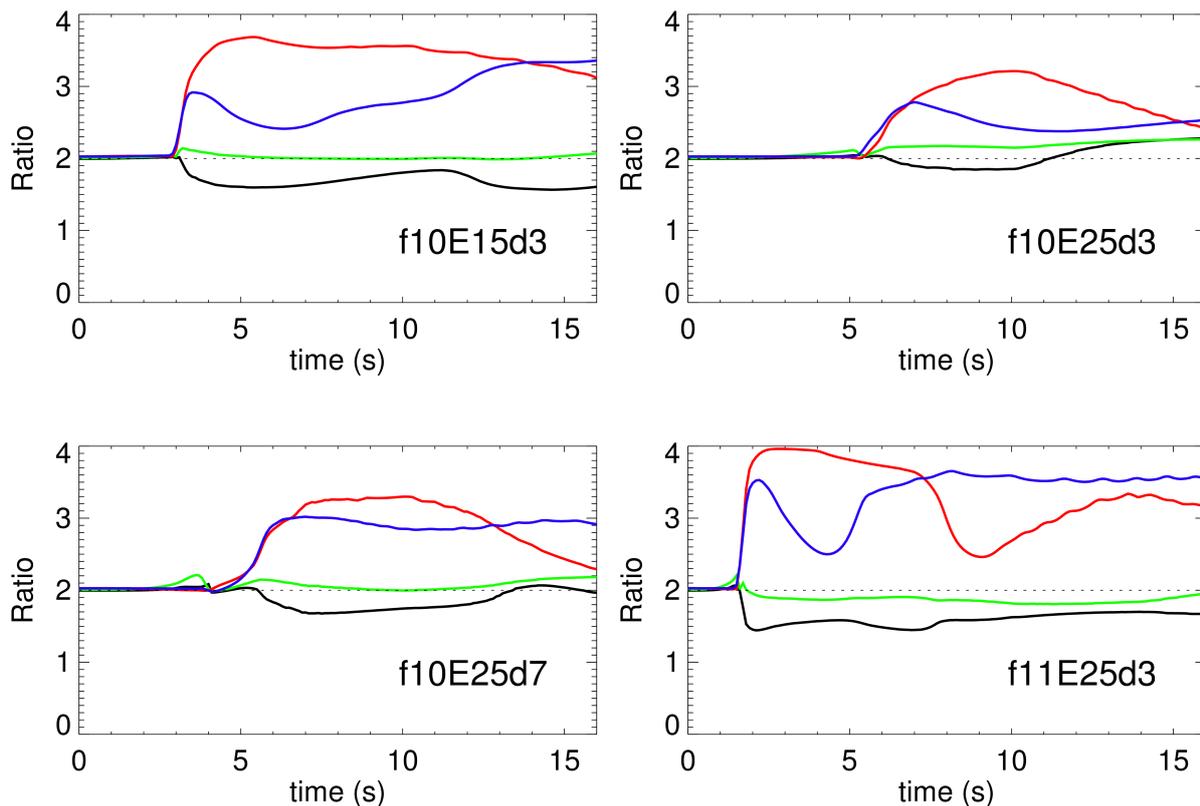
Fig. 3. Time variations of the ratio at the red wing (red solid line), the blue wing (blue solid line), the line core (black solid line) and the ratio of integrated intensity (green solid line) in four cases. The wavelength positions for the line core, the red wing and the blue wing in each case are marked in Figure 1.

the opacity in the line formation region is now non-negligible (Kerr et al. 2019).

We show the intensity ratio profile $r(\Delta\lambda)$ and the optical depth at the line formation height τ_h as functions of wavelength in Figure 5. The formation height is defined as the centroid of the contribution function (Leenaarts et al. 2012).

At $t = 0$ s, τ_h at the line core is smaller than 0.01, which means the opacity effect here is not important, and it is reasonable to treat these lines as optically thin. When the atmosphere is heated during solar flares, τ_h also increases dramatically, especially at the line core. At $t = 10$ s, τ_h is larger than 1 at the line core, corresponding to the rise of the $\tau_\lambda = 1$ curve around the line core in Figure 1. One needs to consider the optical effect at this time although it is still optically thin at the far wings.

The variation of $r(\Delta\lambda)$ seems to be negatively correlated to the variation of τ_h. The intensity ratio $r(\Delta\lambda)$ decreases from the line wings to the line core, while the optical depth τ_h increases. In each intensity ratio profile, the normalized ratio $r_n(\Delta\lambda)$ is defined as: $r_n(\Delta\lambda) = r(\Delta\lambda)/r_{max}$. In Figure 6 we show a scatter plot of the optical depth τ_h and the normalized ratio r_n at each wavelength point at different times from all four simulation cases. A negative tendency is clearly shown in the figure, which implies that the opacity has an obvious effect on decreasing the intensity ratio. We will discuss the reason for this in Section 4.2.

3.3. The population ratio of the Si ɪv 3p levels

The two resonance lines of Si ɪv share the same lower energy level $3s$ but have different higher levels at $3p$. We hereby label the energy levels at $3s$ ($^2S_{1/2}$) and $3p$ ($^2P_{1/2}$ and $^2P_{3/2}$) as levels 0,

1, and 2, respectively, in the order of increasing energies. Thus, the population densities at the three levels are denoted as n_0, n_1, and n_2, respectively. The two $3p$ levels are so close that n_2/n_1 is considered to be the ratio of their statistical weights in LTE assumption (Rathore & Carlsson 2015).

We show the population ratio n_2/n_1 in dependence of height and time in Figure 7, together with the contribution function at the line core. At $t = 0$ s, the population ratio stays close to 2 in the line formation region (around $1.8 − 1.9$ Mm). We notice that in the chromosphere the population ratio is much larger than 2 where there is very little contribution to the line intensity. We will discuss why $n_2/n_1 > 2$ in Section 4.1.

As shown in Figure 1, at around $t = 5$ s, the chromosphere is heated to $\sim 10^4$ K and the Si ɪv line is being enhanced. The contribution function begins to show another peak at around 1.6 Mm from $t = 5.0$ s, and the population ratio above 1.8 Mm starts to increase in the meantime. After $t = 6.0$ s, the contribution function is dominant in the chromosphere, and the population ratio n_2/n_1 is larger than 2 in the layers where the line forms. Checking the results of all four simulation cases, we find an interesting fact that the second C_λ peak and the deviation of n_2/n_1 from 2 are closely related both spatially and temporxally, which also correspond to the enhancement of Si ɪv lines.

4. Discussion

4.1. The deviation of the population ratio from 2

The upper levels of the Si ɪv 1394 Å and Si ɪv 1403 Å lines are the fine structures of Si ɪv $3p$ electron configuration when the
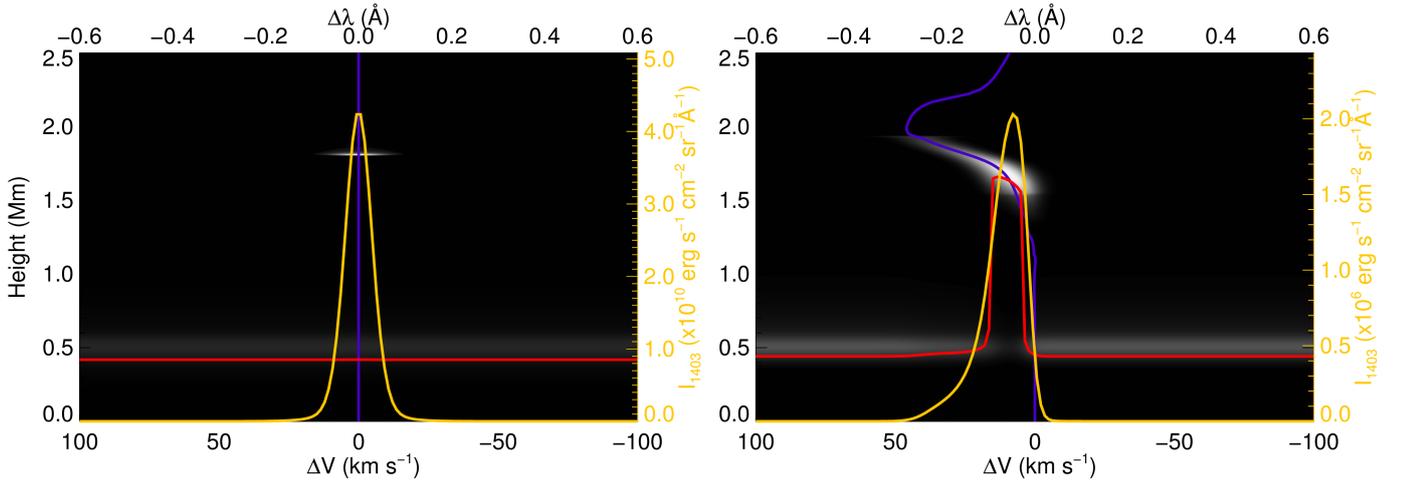
Fig. 4. Line formation of the Si IV 1403 Å line in Case f10E25d3, for $t = 0$ s on the left panel and $t = 10$ s on the right panel. Background gray shades represent the contribution function. Blue lines denote the vertical velocity and red lines denote the $\tau_\lambda = 1$ height. Orange lines refer to the line profiles.
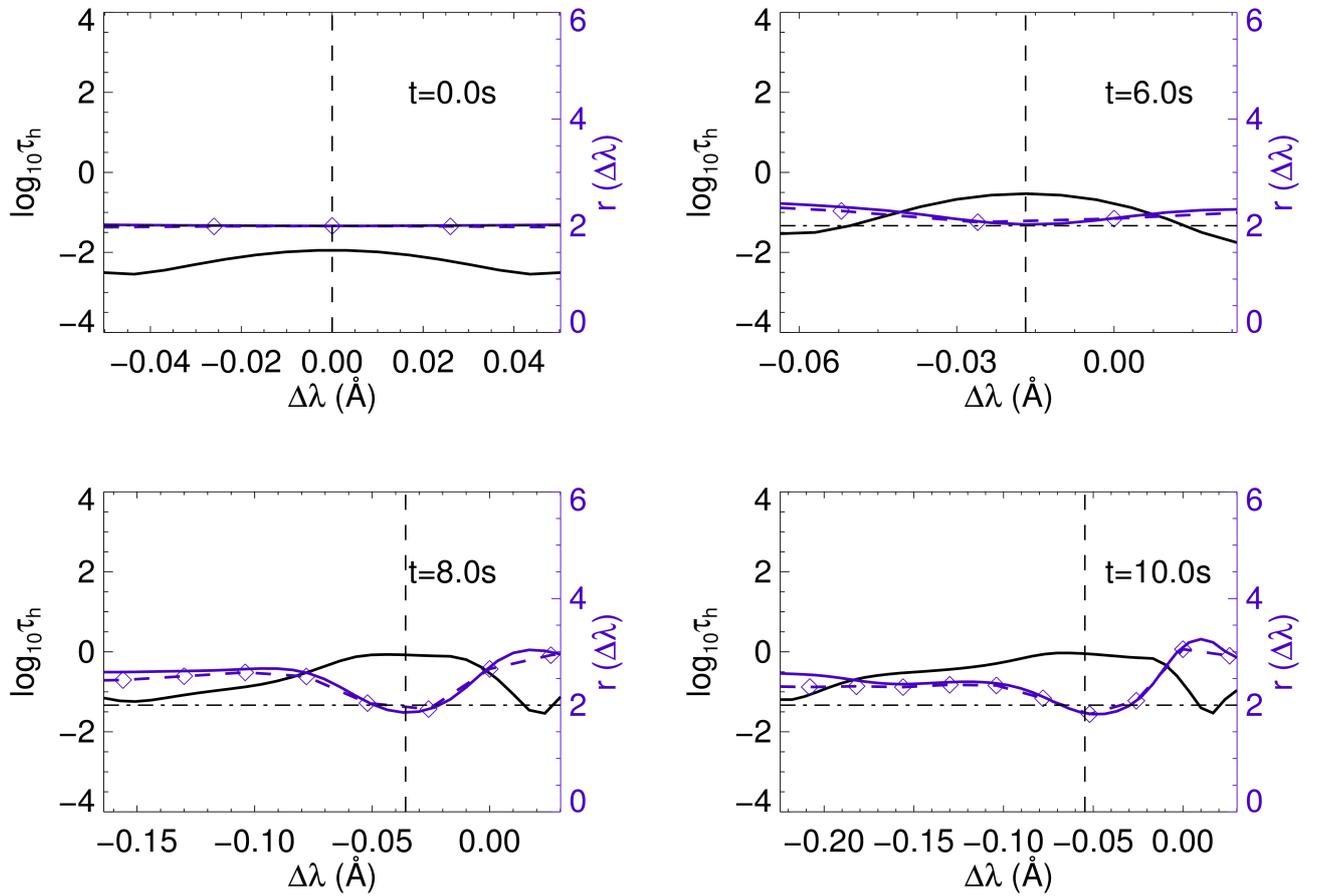
Fig. 5. The optical depth at the line formation height τ_h (black line) and the intensity ratio profile $r(\Delta\lambda)$ (blue solid line) for Case f10E25d3. We only show the wavelength range at which the emergent intensity is larger than three times the continuum. Blue dashed line shows $r(\Delta\lambda)$ that are degraded to the IRIS spectral resolution (0.026 Å). Overplotted are the horizontal line of $r = 2$ and the vertical line for the position of the line core.

degeneracy of the orbital quantum number is broken. The statistical weight is 4 for the $3p\,^2P_{3/2}$ level (the upper level for the Si IV 1394 Å transition), and 2 for the $3p\,^2P_{1/2}$ level (the upper level for the Si IV 1403 Å transition). Under the LTE assumption, the

population ratio n_2/n_1 is described by the Boltzmann equation:

$$\frac{n_2}{n_1} = \frac{g_2}{g_1} e^{-\frac{\Delta\epsilon}{kT}}. \tag{3}$$

where g_1 and g_2 are statistical weights of level 1 and level 2, respectively. The energy level difference $\Delta\epsilon$ is so small that
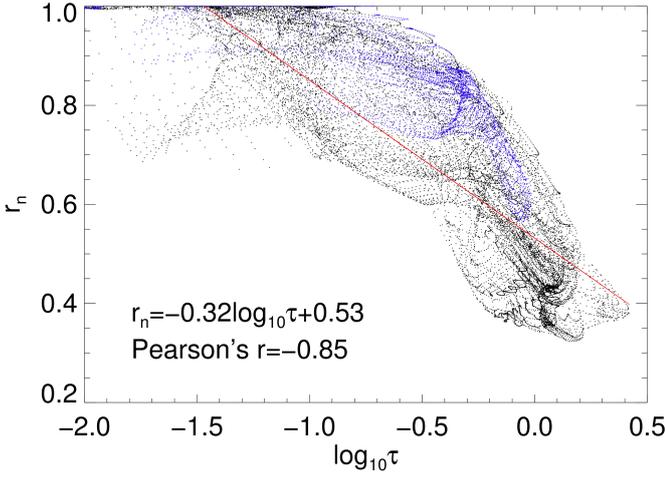
Fig. 6. Scatter plot of the normalized ratio (r_n) versus the optical depth at the formation height (τ_h) for four cases. Blue dots come from Case f10E25d3. The red line shows the result of a linear fit of all the data points.
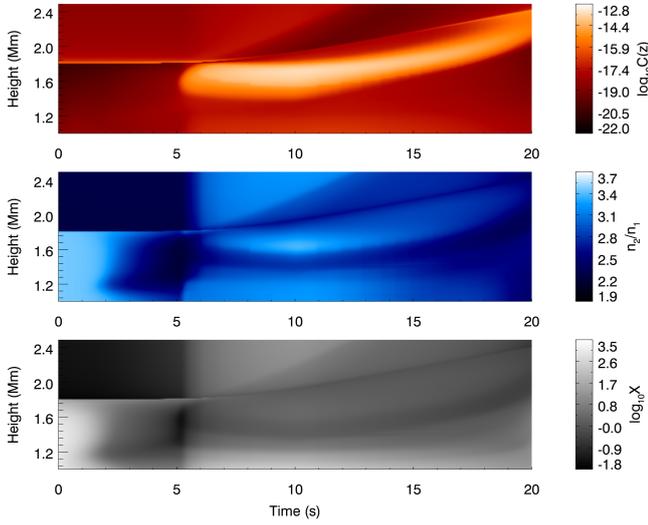
Fig. 7. Time evolution of height distribution of the contribution function at the line core (top panel), the population ratio n_2/n_1 (middle panel) and the proportion of the resonance scattering to thermal emission X (bottom panel) for Case f10E15d3. An obvious enhancement of the contribution function in the chromosphere starts from $t = 5.0$ s.

$e^{-\frac{\Delta\epsilon}{kT}} \sim 1$. Hence, the population ratio n_2/n_1 is considered to be equal to g_2/g_1, which is 2 exactly. However, the LTE assumption is no longer valid above the photosphere. At the chromosphere and the transition region, the non-LTE effect is dominant.

We write the population equations for levels 1 and 2 (the $3p$ levels) as:

$$\frac{dn_1}{dt} = n_0R_{01} + n_0C_{01} + n_2C_{21} + n_cR_{c1} + n_cC_{c1}$$
$$\quad - n_1(R_{10} + C_{10} + C_{12} + R_{1c} + C_{1c}), \quad (4)$$

$$\frac{dn_2}{dt} = n_0R_{02} + n_0C_{02} + n_1C_{12} + n_cR_{c2} + n_cC_{c2}$$
$$\quad - n_2(R_{20} + C_{20} + C_{21} + R_{2c} + C_{2c}), \quad (5)$$

where R_{ij} and C_{ij} denote the radiative and collisional transition rates, and the subscript c represents the continuum level of Si IV.

In Figure 8 we compare all the transition rates in Equation 4 at 6.0 s, where $n_1R_{10} = n_1A_{10} + n_1B_{10}\bar{J}_{10}$. It is very clear that in the line formation region, the transition rates between level 0 and level 1 are orders of magnitude larger than the rates of other transitions. The dominant terms are collisional and radiative excitations plus spontaneous emission. Considering that the time derivatives of the level populations are very small (see Figure 8), we further simplify Equations 4 and 5 by including only the dominant terms:
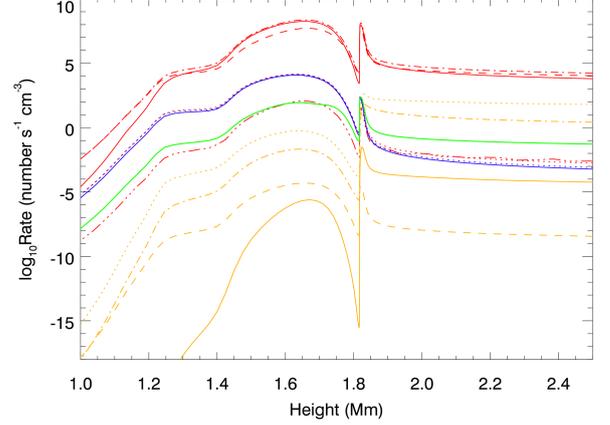
Fig. 8. Height distribution of all the transition rates in Equation 4 for Case f10E25d3 at 6.0 s. Red lines represent transitions between levels 0 and 1: n_0C_{01} (red solid line), n_1C_{10} (red dotted line), n_0R_{01} (red dashed line), n_1A_{10} (red dotted dashed line), $n_1B_{10}\bar{J}_{10}$ (red three-dotted dashed line). Blue lines represent transitions between levels 1 and 2: n_1C_{12} (blue solid line), n_2C_{21} (blue dotted line). Yellow lines represent transitions between level 1 and the continuum: n_1C_{1c} (yellow solid line), n_cC_{c1} (yellow dotted line), n_1R_{1c} (yellow dashed line), n_cR_{c1} (yellow dotted dashed line). The net rate dn_1/dt is plotted as the green line.

$$n_0B_{01}\bar{J}_{01} + n_0C_{01} - n_1A_{10} = 0, \quad (6)$$
$$n_0B_{02}\bar{J}_{02} + n_0C_{02} - n_2A_{20} = 0. \quad (7)$$

The transitions can be divided into two processes: collisional excitation followed by radiative deexcitation, which corresponds to thermal emission; radiative excitation followed by radiative deexcitation, which is referred to as resonance scattering (Gontikakis & Vial 2018). Assuming that $\bar{J}_{02} = (1+k)\bar{J}_{01}$ ($k > 0$) and noticing that $A_{20}/A_{10} = 1$, $C_{02}/C_{01} = B_{02}/B_{01} = 2$, we obtain

$$\frac{n_2}{n_1} = 2 + \frac{2kX}{1+X}, \quad (8)$$

where $X = B_{01}\bar{J}_{01}/C_{01}$ is the proportion of the resonance scattering to thermal emission. We can find that the population ratio is positively correlated with the value of X, that is, the increase of resonance scattering makes $n_2/n_1 > 2$.

The above mechanism is illustrated in the bottom panel of Figure 7. At $t = 0$ s, the radiation is small enough ($X \ll 1$) in the line formation region (1.8 − 1.9 Mm), and the population ratio is 2 according to Equation 8, which is also the result under coronal approximation. After a certain time of flare heating (5 s in Case f10E25d3), the local radiation is enhanced and the radiative excitation rate is comparable to the collisional excitation rate. The population ratio also increases gradually with time and becomes larger than 2 in the line formation region (Figure 7).

4.2. The deviation of the intensity ratio from 2

We now discuss how would the population ratio influences the line intensity ratio. We first consider the optically thin case where the optical depth is so small that $e^{-\tau_\lambda} \approx 1$, and $C_\lambda \approx j_\lambda$. Thus we can obtain the emergent intensity by only integrating the emissivity along the height:

$$I_{1403\text{Å}}(\Delta\lambda) \approx \int j_{1403\text{Å}}(z, \Delta\lambda)\text{d}z = \int n_1(z)A_{10}(z)\psi_{1403\text{Å}}(z, \Delta\lambda)\text{d}z, \tag{9}$$

$$I_{1394\text{Å}}(\Delta\lambda) \approx \int j_{1394\text{Å}}(z, \Delta\lambda)\text{d}z = \int n_2(z)A_{20}(z)\psi_{1394\text{Å}}(z, \Delta\lambda)\text{d}z, \tag{10}$$

where $\psi(z, \Delta\lambda)$ are normalized profiles. Noticing that $A_{20} = A_{10}$, $\psi_{1394\text{Å}}(z, \Delta\lambda) \approx \psi_{1403\text{Å}}(z, \Delta\lambda)$, the ratio of emergent intensity only depends on the population ratio n_2/n_1. At $t = 0$ s, the Si IV lines are optically thin, and the intensity ratio stays close to 2 (Figure 5), which is equal to the population ratio n_2/n_1 (Figure 7).

In flare conditions, we need to consider the optical depth term in the contribution function. The intensity ratio is related to the ratio of the contribution functions since the integration range is the same. The ratio of contribution functions is given as

$$\frac{C_{1394\text{Å}}}{C_{1403\text{Å}}} = \frac{j_{1394\text{Å}}e^{-\tau_{1394\text{Å}}}}{j_{1403\text{Å}}e^{-\tau_{1403\text{Å}}}} = \frac{n_2}{n_1}e^{-(\tau_{1394\text{Å}} - \tau_{1403\text{Å}})}, \tag{11}$$

which is a function of wavelength and height. As we has shown above, deviation of the ratio n_2/n_1 from 2 is mainly from the resonance scattering effect, while the term $e^{-(\tau_{1394\text{Å}} - \tau_{1403\text{Å}})}$ apparently represents the opacity effect. At each height, the ratio of contribution function is reduced by the opacity effect because $\tau_{1394\text{Å}} > \tau_{1403\text{Å}}$. As a result, the intensity ratio is reduced by the opacity effect. However, when the population ratio n_2/n_1 grows due to resonance scattering, the intensity ratio increases proportionally. These two effects compete with each other. Besides their opposite effects on the magnitude of the intensity ratio, the effect of n_2/n_1 is wavelength independent while that of τ is wavelength dependent.

The intensity ratio profiles in Figure 1 could then be explained as follows. The resonance scattering effect elevates the intensity ratio $r(\Delta\lambda)$ to larger than 2, while the opacity effect pulls the ratio back to some extent. At the line center, the opacity is relatively larger so that the intensity ratio is pulled back by a larger amount, causing a U-shaped profile. The ratio at the line wings are generally larger than 2, while the ratio at the line core could be larger or smaller than 2, depending on how much effect the opacity exerts on the ratio.

We further illustrate these two effects by defining the difference of contribution functions as $\Delta C(\Delta\lambda, z) = C_{1394\text{Å}}(\Delta\lambda, z) - 2C_{1403\text{Å}}(\Delta\lambda, z)$. The integration of ΔC along height gives the difference of intensities $I_{1394\text{Å}}(\Delta\lambda) - 2I_{1403\text{Å}}(\Delta\lambda)$. Therefore, the value of ΔC indicates the contribution to the deviation of $r(\Delta\lambda)$ from 2. A positive ΔC tends to elevate $r(\Delta\lambda)$ to over 2, while a negative one tends to suppress $r(\Delta\lambda)$ to below 2.

In Figure 9 we show the distribution of ΔC at $t = 8.0$ s for Case f10E25d3. Note that ΔC is normalized at each wavelength. At each wavelength, the region where $\Delta C > 0$ is located in the upper chromosphere (1.6–1.9 Mm). It is also the line formation
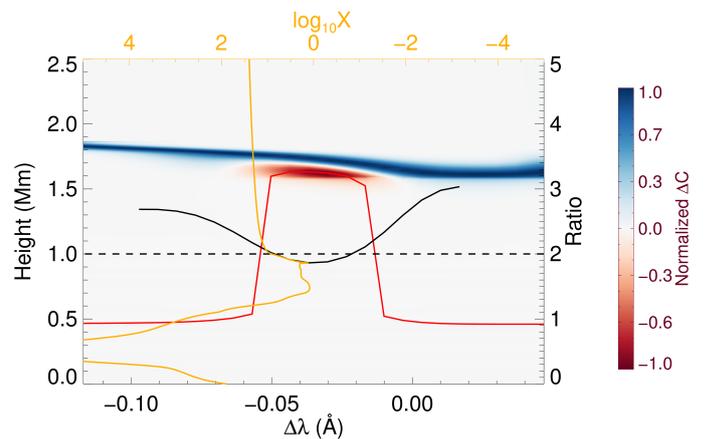
Fig. 9. Normalized difference of contribution functions (ΔC) at 8.0 s in Case f10E25d3 (background). The intensity ratio profile is marked as the black line. The red line denotes the $\tau = 1$ height and the orange line refers to the proportion of resonance scattering to thermal emission (X).

region where the contribution function C_λ is large and resonance scattering is strong ($X > 1$). However, the region where $\Delta C < 0$ only appears in the line core, coinciding with the region with a large opacity.

Thus, the $r(\Delta\lambda)$ profile shows a U-shape, in which the ratio increases towards the line wings but decreases towards the line core. Similar features of $r(\Delta\lambda)$ and ΔC are found in other simulation cases during flare heating.

4.3. Comparison with observations

In Figure 5, we also plot the ratio of the intensity profiles that are degraded to the IRIS spectral resolution (0.026 Å). One can see that the U-shaped profile is still obvious, with the value at the line core smaller than 2, while the value at the line wings larger than 2. Actually, such U-shaped profiles have been reported in previous observations (Zhou et al. 2022).

The central reversal in emission lines is often caused by the large line opacity. In observations there are reports of such features in the Si IV lines, especially in flares (Yan et al. 2015; Zhou et al. 2022; Lörinčík et al. 2022). In our simulations, we find centrally reversed profiles in Case f11E25d3 (Figure 2), where the energy flux F is one order of magnitude higher than that in other three cases. We confirm that the central reversal is due to the increased line opacity.

In many observations of the Sun or other stars, the ratio of integrated intensity R is taken as an indicator of the optical thickness (Mathioudakis et al. 1999; Christian et al. 2006; Yan et al. 2015; Brannon et al. 2015; Mulay & Fletcher 2021). Zhou et al. (2022) claimed that the wavelength-dependent ratio profile $r(\Delta\lambda)$ would be a better indicator since the opacities at the line core and at the line wings are different. Our results confirm that the intensity ratio profile $r(\Delta\lambda)$ usually has a U-shape as in observations. However, we find it still insufficient in some cases to use the value of either R or $r(\Delta\lambda)$ as an indicator of the optical thickness. For example, in the simulation snapshot of Case f10E25d3 at 6.0 s, both R and the intensity ratio at the line core $r(\Delta\lambda_c)$ are larger than 2, but we do see an obvious increase in the line opacity (Figure 5). The normalized ratio r_n might be a complementary indicator of the optical thickness as judged from Figure 6. Quantitatively, the Si IV line is not optically thin any more if $r_n < 0.6$.

5. Conclusions

In this paper, we analyze the properties of the two Si IV resonance lines in flare conditions based on RADYN simulations. We focus on the intensity ratio profile $r(\Delta\lambda)$ and find that the value of $r(\Delta\lambda)$ rises at the line wings and falls at the line core. By comparison, the ratio of integrated intensity R lies between the minimum and maximum of $r(\Delta\lambda)$. At most of the wavelength points, $r(\Delta\lambda)$ deviates from 2 obviously, ranging from 1.5 to 4. However, R usually ranges from 1.8 to 2.3. We agree with Kerr et al. (2019) that the opacity of the two resonance lines are both non-negligible when flare occurs. In the line core, the line opacity is larger and $r(\Delta\lambda)$ becomes smaller than that in the line wings. By calculating the normalized ratio $r_n(\Delta\lambda) = r(\Delta\lambda)/r_{\max}$, we can quantitatively estimate the optical depth at the line formation height through an empirical relationship between r_n and τ (Figure 6).

We also find that due to flare heating, the increased rate of resonance scattering will increase the population ratio of the Si IV $3p$ levels (n_2/n_1), which will in turn increase the intensity ratio $r(\Delta\lambda)$. In the mean time, the large opacity at the line core tends to decrease the intensity ratio $r(\Delta\lambda)$. The competition of the resonance scattering effect and the opacity effect will result in a U-shaped intensity ratio profile as in observations.

As noted above, the values of R and $r(\Delta\lambda)$ are influenced by both resonance scattering and opacity. In the case that R and $r(\Delta\lambda)$ are not sufficient to judge the optical thickness, we propose to use the normalized ratio $r_n(\Delta\lambda)$ as a complementary criterion. We conclude that if $r_n < 0.6$, the line should be regarded as optically thick. Such a case most likely appears at the line core. On the other hand, since the opacity at the far wings is always small, deviation of the intensity ratio $r(\Delta\lambda)$ from 2 can safely serve as an indicator of the strength of resonance scattering.

References

Allred, J. C., Kowalski, A. F., & Carlsson, M. 2015, ApJ, 809, 104
Brannon, S. R., Longcope, D. W., & Qiu, J. 2015, ApJ, 810, 4
Caccin, B., Gomez, M. T., Marmolino, C., & Severino, G. 1977, A&A, 54, 227
Carlsson, M. & Stein, R. F. 1992, ApJ, 397, L59
Carlsson, M. & Stein, R. F. 1995, ApJ, 440, L29
Carlsson, M. & Stein, R. F. 1997, ApJ, 481, 500
Christian, D. J., Mathioudakis, M., Bloomfield, D. S., et al. 2006, A&A, 454, 889
Dorfi, E. A. & Drury, L. O. 1987, Journal of Computational Physics, 69, 175
Gontikakis, C. & Vial, J. C. 2018, A&A, 619, A64
Gontikakis, C., Winebarger, A. R., & Patsourakos, S. 2013, A&A, 550, A16
Hong, J., Carlsson, M., & Ding, M. D. 2022, A&A, 661, A77
Kerr, G. S., Carlsson, M., Allred, J. C., Young, P. R., & Daw, A. N. 2019, ApJ, 871, 23
Leenaarts, J., Carlsson, M., & Rouppe van der Voort, L. 2012, ApJ, 749, 136
Li, Y., Ding, M. D., Hong, J., Li, H., & Gan, W. Q. 2019, ApJ, 879, 30
Lörinčík, J., Polito, V., De Pontieu, B., Yu, S., & Freij, N. 2022, Frontiers in Astronomy and Space Sciences, 9, 1040945
Magain, P. 1986, A&A, 163, 135
Maniak, S. T., Träbert, E., & Curtis, L. J. 1993, Physics Letters A, 173, 407
Mathioudakis, M., McKenny, J., Keenan, F. P., Williams, D. R., & Phillips, K. J. H. 1999, A&A, 351, L23
Mulay, S. M. & Fletcher, L. 2021, MNRAS, 504, 2842
Nelson, C. J., Freij, N., Reid, A., et al. 2017, ApJ, 845, 16
Rathore, B. & Carlsson, M. 2015, ApJ, 811, 80
Reid, A., Zhigulin, B., Carlsson, M., & Mathioudakis, M. 2020, ApJ, 894, L21
Tian, J., Hong, J., Li, Y., & Ding, M. D. 2022, A&A, 668, A96
Tripathi, D., Nived, V. N., Isobe, H., & Doyle, G. G. 2020, ApJ, 894, 128
Yan, L., Peter, H., He, J., et al. 2015, ApJ, 811, 48
Zhou, Y.-A., Hong, J., Li, Y., & Ding, M. D. 2022, ApJ, 926, 223

Appendix A: Additional Simulation Cases

Table A.1. Additional 22 simulation cases

Case	F_{peak}/[erg s^{-1} cm^{-2}]	E_c/[keV]	δ
f10E05d3		05	3
f10E10d3		10	3
f10E20d3		20	3
f10E05d4		05	4
f10E10d4		10	4
f10E15d4		15	4
f10E20d4		20	4
f10E25d4		25	4
f10E05d5		05	5
f10E10d5		10	5
f10E15d5	10^{10}	15	5
f10E20d5		20	5
f10E25d5		25	5
f10E05d6		05	6
f10E10d6		10	6
f10E15d6		15	6
f10E20d6		20	6
f10E25d6		25	6
f10E05d7		05	7
f10E10d7		10	7
f10E15d7		15	7
f10E20d7		20	7

Appendix B: Additional Figures
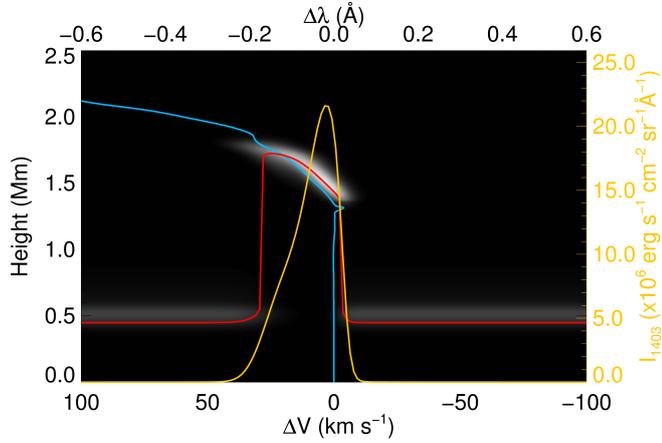
Fig. B.1. The same as Figure 4 but for Case f10E15d3 at t = 10 s.
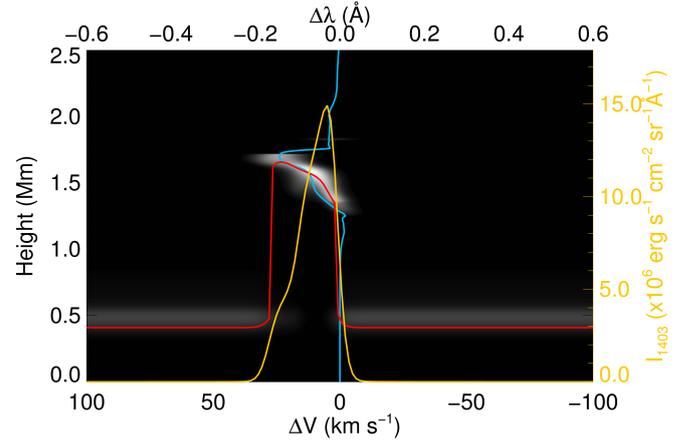
Fig. B.2. The same as Figure 4 but for Case f10E25d7 at t = 10 s.
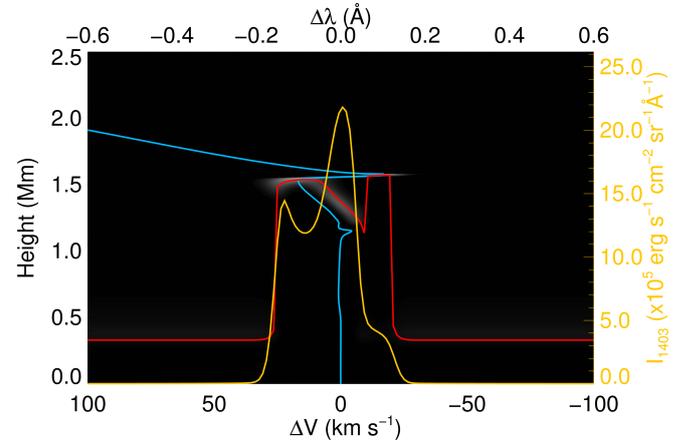
Fig. B.3. The same as Figure 4 but for Case f11E25d3 at t = 10 s.
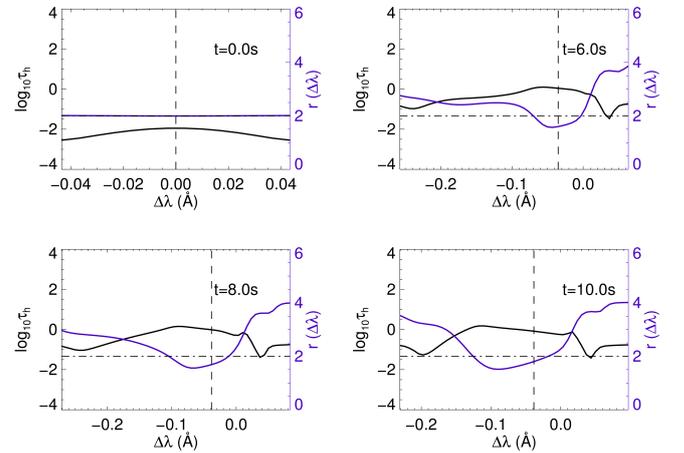
Fig. B.4. The same as Figure 5 but for Case f10E15d3.
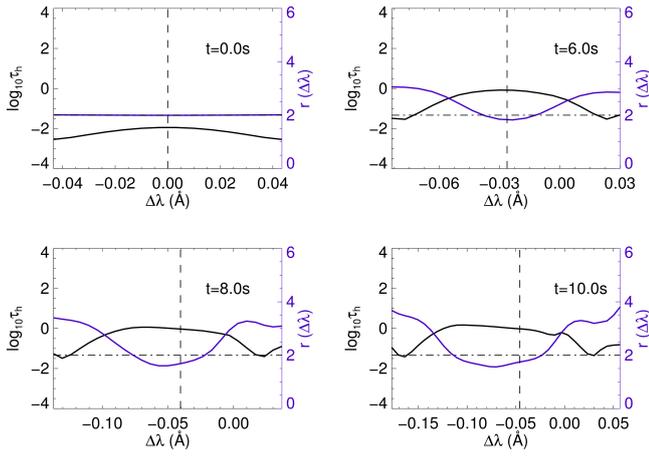
Fig. B.5. The same as Figure 5 but for Case f10E25d7.

Fig. B.6. The same as Figure 5 but for Case f11E25d3.

Fig. B.7. The same as Figure 7 but for Case f10E15d3.

Fig. B.8. The same as Figure 7 but for Case f10E25d7.

Fig. B.9. The same as Figure 7 but for Case f11E25d3.
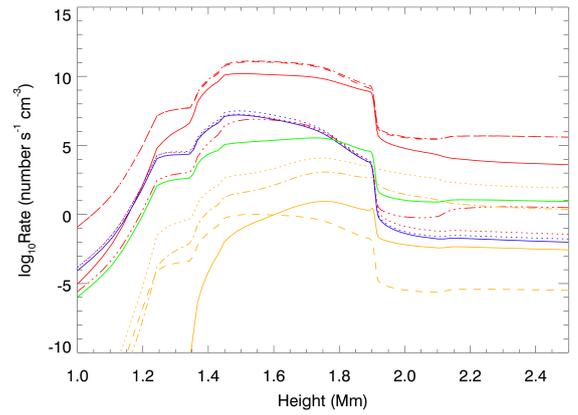
Fig. B.10. The same as Figure 8 but for Case f10E15d3.
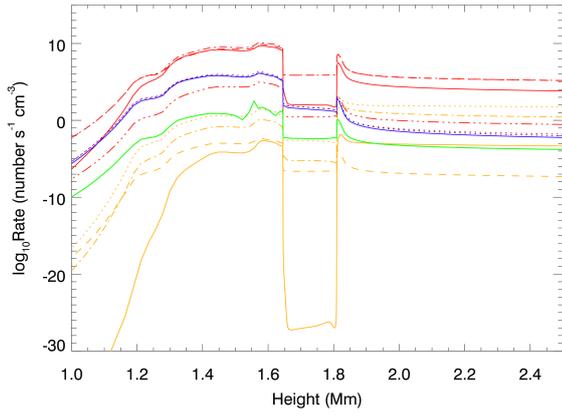
Fig. B.11. The same as Figure 8 but for Case f10E25d7.

Fig. B.12. The same as Figure 8 but for Case f11E25d3.

Fig. B.13. The same as Figure 9 for Case f10E15d3.
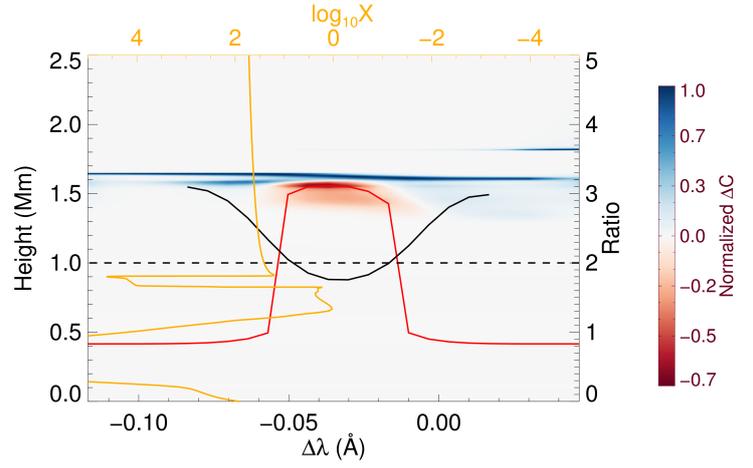
Fig. B.14. The same as Figure 9 for Case f10E25d7.
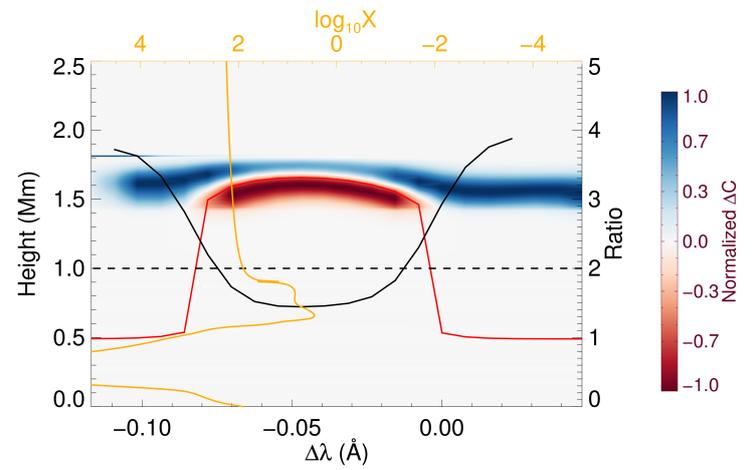
Fig. B.15. The same as Figure 9 for Case f11E25d3.